Supplementary Materials for

Aerial Photographs Reveal Late–20th-Century Dynamic Ice Loss in Northwestern Greenland

Kurt H. Kjær,* Shfaqat A. Khan, Niels J. Korsgaard, John Wahr, Jonathan L. Bamber, Ruud Hurkmans, Michiel van den Broeke, Lars H. Timm, Kristian K. Kjeldsen, Anders A. Bjørk, Nicolaj K. Larsen, Lars Tyge Jørgensen, Anders Færch-Jensen, Eske Willerslev

*To whom correspondence should be addressed. E-mail: kurtk@snm.ku.dk

Published 3 August 2012, *Science* **337**, 569 (2012)
DOI: 10.1126/science1220614

This PDF file includes:

Materials and Methods

Surface elevation data

Aerial photographs - GR96 ground control - 1985 DEM

Between 1978 and 1987, the Danish National Survey and Cadastre (KMS, then Geodætisk Institut) covered all ice-free areas of Greenland, including nunataks, with black-and-white aerial stereo-photography. The photography extended across wide parts of the GrIS, as well. Later, the photographs were aero-analytically triangulated using a subset of the geodetic stations of the GR96 reference system(*31*).

The Greenlandic reference system GR96 is the fundamental 3D-reference system in Greenland and is determined from a global reference system used in conjunction with GPS-surveying.

In the 1990s the need for a more accurate reference system in Greenland became evident through the common use of GPS. Thus the new reference system REFGR was established(*32*,*33*). This reference network is measured using GPS and defines the official geodetic reference system in Greenland. GR96 is determined in practice by the points in the reference network REFGR which have been surveyed by GPS and the coordinates then calculated from international permanent GPS reference stations. The coordinates for these stations are given in the global reference frame 15/8 1996 ITRF94 (International Terrestrial Reference Frame). GR96 covers Greenland in its entirety.

This reference frame and this time were chosen since the first points were surveyed in august 1996 and the current reference frame at that time was ITRF94. Thus, the coordinates for the REFGR points are “fixed” to the time 15/8 1996 in ITRF94, defining the reference system GR96, which is the fundamental reference system in Greenland. More than 6000 points have been surveyed in Greenland, mainly using terrestrial methods. At a few of these points, astronomical observations were made to locate the reference system in relation to the centre of the earth.

The GR96 reference system was expanded to the triangulation network. Approximately 100 points in the triangulation network have also been surveyed by GPS. The coordinates determined by GPS are far more accurate than the coordinates determined from the triangulation.

When the GPS-surveyed coordinates are introduced into a recalculation of the triangulation network a far better determination of the points is provided, just as GR96 is transferred to the triangulation points. The result is a net of c. 6000 points updated to the latest reference system GR96.

The accuracy of GPS determined points is 1-2 cm for the oldest points, while the rest have an expected accuracy of 3-4 cm. The accuracy of the recalculated triangulation points is c. 25 cm for points in the central parts of the network and points on the edge have an accuracy of c. 75 cm.

There is at least two REFGR points in each of the 85 towns and hamlets, however a number of points have also been established on selected sites away from inhabited areas.

In winter, 2006 all Doppler observations included in the first aero-triangulation were recalculated, new were added and the aero-triangulation was recalculated, resulting in coordinates in the new datum GR96. A subset of the geodetic stations was used for the aero-analytical triangulation, supplemented with a number of

same heights and zero heights for additional control. The weights in the adjustment are in general 8 m for coordinates and 3.5 m for heights.

Photographs covering our region of interest - northwest Greenland – were recorded in 1985 to a scale of 1:150,000. These were scanned to a resolution of *c.* 15 µm on the film roll, which means a pixel corresponds to a ground resolution of *c.* 2 m. This was done on a photogrammetric scanner with a geometric error of 1-3 µm RMS. We used a total of 210 photographs of scale 1:150,000 to cover the study area and to produce a DEM (Digital Elevation Model) for 1985. This coverage enabled us to model 16729 km2 of the GrIS margin (Fig. S1a). Thus, the source material for the 1985 DEM was the precision-scanned aerial photos with their respective camera calibration reports, and GR96 coordinate lists with corresponding image observations. We carried out the work with the softcopy photogrammetric application SOCET SET 5.5 from BAE SYSTEMS.Interior orientation of the images (image to sensor registration) was done with the corresponding calibration data. We obtained a priori camera positions and attitudes (exterior orientation) with the flight line maps as the primary source. We organized photographs and supporting data in the Multi-Sensor Triangulation module of SOCET SET, then bundle block adjusted/triangulated using a rigorous simultaneous solution. For automated measurement and collection of elevation points to a gridded DEM, the NGATE (Next Generation Terrain Extraction) module of SOCET SET was employed(*34*). The adaptive (ngate.strategy) and low contrast (ngate_low_sp.strategy) strategies were used with a ground sample distance (GSD) of 25 m. The latter strategy is better at sampling elevations in low-contrast areas (snow). Both strategies have *c.* three dozen adjustable parameters, two of which will be mentioned here: image correlation window size and image correlation cutoff value. The image correlation window size is the dimension of the correlation bitmap; the two strategies have default window sizes of 13 and 15 pixels (26 m and 30 m). Thus, the elevation is measured with windows of 26 m x 26 m and 30 m x 30 m size for every pixel, and the 25 m grid cell elevation is calculated from these. BAE SYSTEMS claims NGATE DSMs and LIDAR DSMs have similar accuracy for natural [bare earth] terrain, though dependent on relative flying heights of image and LIDAR acquisition missions(*34*). The elevation with the best quality from the two strategies is retained. The cutoff image correlation value is 0.70 for both strategies. All the settings in NGATE were set for obtaining the best quality at the expense of computing time. The DTM filters were set to DSM (Digital Surface Model) as there are virtually no man-made structures, nor significant vegetation in Greenland. Thus, no post-processing is needed, since the DSM is the DEM. We manually cut areas out of the model where the collection of elevation points failed, as did we cut out all nunataks including a 100 m buffer zone around these. Ortho-mosaics of the region were produced using the registered 1985 photos and the gridded 1985 DEM for reprojection.

1985 DEM accuracy assessment

We assessed the accuracy of the 1985 DEM elevations using airborne laser altimetry data from the period 1993 to 2010 as the reference. These were collected with the Airborne Topographic Mapper (ATM) mounted on a NASA P-3 and have an elevation uncertainty of σ_{ATM} = 0.1 m. However, up to 1995 they had an uncertainty of σ_{ATM} = 0.2 m(*35*), though only a fraction of the data were recorded prior to 1995. This makes the ATM data suitable as reference data, as

they are an order of magnitude more accurate than that expected from a DEM produced from scale 1:150,000 black-and-white aerial photos scanned to a 2 m ground resolution. Recommendations from the National Digital Elevation Program (NDEP)(*36*) are that the reference data should be an independent source of at least three times greater accuracy than the data tested. The ATM spot diameter is *c.* 1 m which is also an order of magnitude less than the spatial extent of the 25 m x 25 m grid cells.

We filtered the ATM data, so that only observations on stable terrain (e.g. bedrock) were kept in the analysis: observations on ice, snow, oceans and lakes were manually deleted by visually inspecting the ATM data superimposed on the orthophoto-mosaics. Furthermore, we included only ATM observations with a corresponding measured observation in the 1985 DEM. Finally, we manually inspected the observations with the largest residuals for gross errors, which were typically due to errata in the ATM data, and to a lesser extent in the 1985 DEM measurements; the inspected group was small, totaling *c.* 500 observations, most of which were removed. The largest residuals caused by random errors seem to be *c.* 55 m, while gross errors are in the hundreds of meters. Only 186216 of the available 337783 observations were retained for further analysis, most of which were deleted due to not full-filling the requirement of not being sampled on bedrock. NDEP(*36*) emphasizes that check points should never be located in terrain with slopes greater than 20 degrees, because in that case the horizontal positional errors would unduly influence the vertical error assessment. Filtering to remove observations with slopes greater than 20 degrees left 170884 sample points.

The 1985 DEM-ATM test results are presented in Figs. S2a-f; these are the residuals which have not been filtered for slope, but only generalized into statistics on 500 x 500 m cells . At Wolstenholme Fjord (Thule AFB) the distribution of ATM flight paths is atypical, because Thule AFB was one of the three base sites for the survey aircraft (Søndre Strømfjord and Kulusuk were the other two). Additionally, the ramp and tarmac were used to validate the survey instrument; note the extreme point density on the ramp and tarmac in Fig. S2c; more than half the testing points of the study area are shown in this figure.

To find the best representative vertical uncertainty, a correction for this spatial skewing or bias is applied; the slope-filtered data were spatially normalized by summarizing the means and standard deviations of 500 m cells, thereby removing most of the spatial bias of the sample point distribution. We reduced the 170884 observations to 2862 (500 m cells). The result for the non-slope-filtered and non-spatial bias corrected test is: minimum -51.2 m; maximum 50.2 m; mean -0.7 m; standard deviation 5.6 m. The result for the slope-filtered, spatial bias corrected test is: minimum – 32.8 m; maximum 30.8 m; mean -0.5 m; standard deviation 5.5 m (fig. S3a; S3b).

For the region of interest the fundamental vertical uncertainty becomes $\sigma_{terrain}$ = 5.5 m, with a bias of -0.5 m to be applied to dh calculations. This corresponds to a correction of +9.0 km^3 for the entire 16729 km^2 when synthesized with observations and results derived independently from the 1985 DEM. Although this fundamental vertical uncertainty could be considered a supplementary uncertainty by virtue of its well-defined land coverage definition, it will be shown that $\sigma_{terrain}$ = 5.5 m is larger than the result for the one major excluded land coverage type: glacier ice, which is the land coverage component of interest in

this paper. Thus, it is a conservative error estimate, and we adopt it as the fundamental vertical uncertainty.

Based on the same series of scale 1:150,000 aerial photos and digital photogrammetric software (Socet Set and NGATE), but using alternate field surveyed ground control, Motyka *et al*.(*37*) estimated the uncertainty to be 2.8 m with a positive bias of 0.7 m. This was done with ATM data filtered for slope as the reference. However, they chose a conservative estimate of 5.6 m in their subsequent analysis.

The uncertainty deteriorates with high slope and abrupt changes in the landscape, or large surface roughness, which is clearly recognizable in Fig. S2a. Escarpments along coasts or glacier carved valleys are prominent with values greater than 3σ. Large means are evident at this location as well (Fig. S2b). The uncertainty also varies greatly in the eastern region, where Fig. S2b, suggests a fairly large systematic bias. This, however, can be rejected based on the large variation of uncertainty and mean (Figs. S2a; S2b), which most likely indicates a challenging topography for this method of evaluating uncertainties (fig S3c; S3d).

Tasiusaq Bugt is a region where the ATM-tracks on the ice-free terrain are clearly discernible and the point distribution is typical (Figs. S2d-f), the latter contrasts highly with the high sample density in Wolsteholme Fjord. The variation in the uncertainty is less, and locally uniform. Higher uncertainties can be observed on escarpments on coasts and nunataks. Local means are gently undulating from south to north, from intervals of [-5.6; -2.9] m to [2.9; 5.6] m (Fig. S2e). The gradual shift of the mean (bias) and the small variation in the uncertainties indicate that this is a systematic error, or bias. Such undulations are to be expected in large-scale aero-analytical triangulations. Applying the bias correction of -0.5 m removes most of the error introduced from this phenomenon in calculations pertaining to the GrIS coverage in the study area.

The fundamental vertical uncertainty was found to be $\sigma_{terrain}$ = 5.5 m for the study area. The residuals are determined by subtracting the ATM reference data from the interpolated surface of the 1985 gridded DEM, and are valid for the ice- and snow-free areas used in the test. Yet a supplemental vertical uncertainty for the land coverage category of glacier ice is desirable for our study, and it is this result which will be used as the uncertainty of the 1985 DEM on glacier ice in this study.

No practical reference data exist for such a test, though it can be modeled from the expectation that the uncertainty is a function of slope(*38*,*39*). This is also the case for the 1985 DEM (Fig. S3e). Briefly, the supplementary uncertainty was estimated by applying the relationship between slope/uncertainty, which was found by testing the ice-free land coverage, to the slope frequency distribution of the glacier ice land coverage (Figs. S3e). In practical terms, this is a normalization of the two land coverages, eliminating the variable effect from different slope distributions. This supplementary vertical uncertainty is found to be σ_{ice} = 4.1 m, which has been applied to our uncertainty estimates of volume change, $\sigma_{DEM1985}$.

The above transformation excludes all slopes of 20 degrees or more, but still accounts for 98.5% (Fig. S3e) of the glacier ice area investigated; the final 1.5% can be considered outliers, though they still present a good fit. Our frequency distribution of the slope of the GrIS margin is much different compared to existing analysis, which show maximum slopes in the single digits(*40*). In this case, the modus of Yi *et al*.(*40*) uses the roughness to describe the variability of

the margin. This roughness is reflected in our much higher resolution data as higher slopes.

ICESat and ATM data

We use ICESat GLA12 Release 31 data(*14*), to resolve elevation changes relative to 1985 (Fig S1). The Geoscience Laser Altimeter System (GLAS) instrument on ICESat provides measurements of ice sheet elevations(*14*). We obtained ICESat elevations (release 31) from the National Snow and Ice Data Center. The ICESat elevations are provided on the TOPEX/Poseidon ellipsoid, and were converted to the WGS84 ellipsoid. The satellite laser footprint diameter is 30-70 m and the distance between footprint centers is approximately 170 m.

The dominant biases on ICESat elevations come from pointing errors and saturation errors. However, pointing errors are now largely corrected in calibration(*41*,*42*). Signal saturation can cause heights to be biased low by up to 1.5 m (*42*). Applying a saturation correction to the height reduces these errors(*14*). A further bias can appear as prominent height anomalies that vary locally when clouds are present (-0.16 m through thick cirrus clouds(*14*)). We use the difference between the shape of the return signal and a Gaussian fit (the IceSvar parameter) to reject less reliable data. Large differences indicate less reliable surface elevation estimates. Measurements for which the misfit is large (IceSvar > 0.03) are rejected. Multiple peaks can be caused by cloud reflection. Waveforms that contain more than one peak in the return signal are rejected from the analysis. For ICESat elevations that have been corrected for pointing errors and saturation errors, and that have been filtered for surface roughness and atmospheric scattering, the single-shot accuracy is σ_{ICESat} = 0.2 m(*5*,*14*,*43*). As a complement to the ICESat data, we use ATM observations taken along flight-lines in this region for 2005 and 2010. The ATM measurements have an elevation accuracy of σ_{ATM} = 0.2 m (*35*).

Elevation difference

To estimate elevation changes, we use ICESat and ATM track points that are less than 17 m from the nearest 1985 DEM point. Consequently, errors caused by the surface slope can be ignored. Each thinning value between an ICESat (or ATM) track point and the nearest 1985 DEM point has an uncertainty of:

$$\sigma_{thinning} = \sqrt{\sigma_{DEM1985}^2 + \sigma_{ICESat}^2} = 4.1 \text{ m}$$

Figure 2a-b shows interpolated thinning values (on a 25x25 m grid) during 1985-2005 and 1985-2010. The interpolation is performed using the kriging method(*44*) and using the GRAVSOFT software package(*45*). We use the observed thinning values with their associated uncertainty of 4.1 m to interpolate thinning values on a 25 x 25 m grid. For each grid point, *i*, we interpolate a thinning value dh_{interp}^{i} and estimate an associated uncertainty σ_{interp}^{i}. Figure S4 shows predicted uncertainties associated with the interpolated thinning values shown in figures 2a-d.

Catchment-wide ice loss

We use time-dependent gravity data from the GRACE satellite mission, to estimate the rate of mass loss across Greenland. The gravity data are available in the form of monthly sets of spherical harmonic coefficients. We use coefficients provided by the Center for Space Research at the University of Texas. We replace the GRACE C_{20} coefficients with those estimated from satellite laser ranging(*46*), and include degree-one terms computed as described by Swenson *et al.*(*47*) (provided by Sean Swenson). We use methods described in Wahr *et al.*(*25*) to transform the gravity coefficients into surface mass coefficients, and use those coefficients to compute surface mass on a 0.5 x 0.5 degree grid, smoothed with a Gaussian smoothing function with a 250-km half-width. The GRACE(*48,50*) and InSAR data(*51*) shows that a considerable increase in the mass loss rate and glacier speed occurred in southeast Greenland in late 2003, attributed both to enhanced melting and increased dynamic ice loss(*6*). Even though GRACE observations show that the mass loss of the entire ice sheet is still accelerating(*9*), they also indicate a deceleration occurred in 2006 in the southeast (Fig. 1). The deceleration is further confirmed by GPS observations(*8*) and ASTER (Advanced Spaceborne Thermal Emission and Reflection Radiometer) data from the TERRA (EOS AM-1) satellite mission(*7*) suggesting this deceleration in ice loss and glacier speed was synchronous for several outlet glaciers along the southeast margin. A similar, but later, speed-up has been noted along the northwest margin(*10*).

Surface Mass Balance

The Regional Atmospheric Climate MOdel v.2 (RACMO2) is based on the High Resolution Limited Area Model (HIRLAM) with physical processes adopted from the global model of the ECMWF. Its adaptation for the Greenland ice sheet, including the treatment of meltwater percolation and refreezing, as well as the evaluation of the modelled SMB(*16-18*). The lateral boundary conditions are provided by ECMWF re-analyses: a combination of ERA-40 (until 2002) and operational analyses (after 2002).The model is run over the 1958-2010 period. Based on a comparison with observations, Ettema *et al.*(*16)* concluded that the model performs very well (N = 265, r = 0.95), yielding a 14 % uncertainty in ice sheet integrated SMB.

SMB from RACMO was converted to SMB induced elevation change using a simple firn model(*19*). The model used annual values of temperature, accumulation, melt and refreezing from RACMO as input. For every year, *SMB* is calculated as the sum of accumulation and refreezing minus melt, all with units [m ice a^{-1}]. The model assumes that all processes take place in the surface layer (i.e., no meltwater percolation). The surface layer contains a fraction of snow, and, where melt and refreezing occur, a fraction of refrozen ice. The layer of refrozen ice that remains at the end of the melt season (hereafter referred to as SIR; Superimposed Ice Remaining) is equal to the refreezing from RACMO, albeit constrained to be between zero and SMB. Based on SMB and SIR three zones can be distinguished: the ablation zone (SMB < 0, SIR=0), the dry-snow zone (SMB > 0, SIR=0) and the percolation zone ($SMB \geq SIR > 0$). In the ablation zone, the elevation change due to SMB is simply equal to SMB as glacier ice is melted. For the percolation and dry-snow zones, the density is not equal to that of ice and is modeled as follows.

Based on near-surface depth density data and firn temperatures, Reeh *et al.*(20) showed that the surface snow density can be calculated by:

$$\rho_{s0} = 625 + 18.7T_f + 0.293T_f^2$$

where T_f is the firn temperature at 10m depth in °C, which depends on the mean annual temperature *TMA*, and *SIR*(*52*):

$$T_f = TMA + 26.6SIR$$

As the surface layer is covered by subsequent layers firn compaction occurs, and hence the density of the firn fraction will increase and the thickness of the layer will decrease. The thickness of the annual layer *D*, which is deposited at time t_0, after *t* years of compaction, will be(*19*):

$$D(t_0, t) = SMB(t_0)\frac{\rho_i}{\rho_{s0}(t_0, t)} + SIR(t_0)(1 - \frac{\rho_i}{\rho_{s0}(t_0, t)})$$

where ρ_i is the density of ice (917 kg m^{-3}), and $p_{s0}(t_0,t)$ is the density of the firn fraction of layer *D* after *t* years of compaction. To model the firn compaction process, the parameterization by Zwally and Li(*53*) was used:

$$\rho_s(t_0, t) = \rho_i - (\rho_i - \rho_{s0}(t_0))e^{-ct}$$

c is given by:

$$c = \overline{SMB}\left(\frac{\rho_i}{\rho_w}\right)\left(139.21 - 0.542\left(\overline{T_f} + 273.15\right)\right)(8.36\left(273.15 - \overline{T_f}\right)^{-2.061}$$

where ρ_w is the density of water (1000 kg m^{-3}) and $\overline{SMB}$ and $\overline{T_f}$ are the long-term average surface mass balance and firn temperature, respectively. Interannual fluctuations temperature and accumulation are thus only taken into account for the surface layer and neglected in the modeling of the compaction process.

The elevation change induced by SMB is taken as the anomaly of the thickness of the surface layer $D(t_0)$ with respect to the reference surface layer thickness (the 1961 to 1990 average). The total firn profile thickness at a given time is calculated as the sum of the thickness of 99 annual layers (not the surface layer) that each have compacted for the appropriate amount of time. For example, the profile thickness D_T in 1985 is calculated as:

$$D_T(1985) = D(1958{,}27) + D(1959{,}26) + \cdots + D(1984{,}1) + \sum_{i=28}^{99} D(ref, i)$$

Because the RACMO run started in 1958, the upper 27 layers were modelled, and the profile was completed using the lower 72 layers from the reference profile (*D(ref,i);* 1961-1990 average profile). The largest firn compaction rates will occur in the upper layers, therefore the error introduced by assuming a partial reference profile will be minor. As more modeled layers become available later in the period of interest, this initialization error decreases. When the ice sheet is in balance, firn compaction does not cause a surface elevation change. Thus, the elevation change due to firn compaction is again the anomaly of the profile thickness with respect to the 1961-1990 average (i.e., the total thickness of the reference profile).

To estimate the errors in elevation changes due to SMB and firn compaction, we started from the accuracy of SMB and temperature as produced by RACMO, and

propagated the uncertainty through the model. According to Ettema *et al.*(*17,18*) the average temperature bias over the entire GrIS is +0.9°C, and we chose a value for the random error (RMSE) of 2.5°C, which is slightly higher than the estimate by Ettema *et al.*(*17,18*) over both ice sheet and land area. Prior to running the firn model, temperature from RACMO was corrected for this bias by subtracting 0.9°C. The accuracy of *SMB (ΔSMB)* as simulated by RACMO(*16*) is:

$$\Delta SMB = 15 + 0.01SMB + 0.0002SMB^2$$

Here, *SMB* is in kg m^{-2} yr^{-1}, with a maximum for *ΔSMB* of 30% of *SMB*. However, this holds only for the accumulation zone. In the ablation zone, the alleged value is 20% of *SMB*(*16*). Because we did not have information about refreezing, we used the same value (20%) for the *SIR* content in each annual layer. Next, we ran the firn model with high (plus error) and low (minus error) estimates of both SMB and temperature. The provided errors in elevation changes are the maximum absolute differences between these four model runs and the baseline run.

Ice marginal changes

Frontal changes in Northwest Greenland 1985-2010

To compare observations of glacier elevation changes with changes in the position of the entire ice sheet margin, we map the fronts at three different dates in the observation period 1985-2010. The first date is 1985, mapped from the orthorectified photo mosaic created with the 1985 DEM. The following dates (2005 & 2010) are mapped from Landsat ETM+ images downloaded from the USGS online archive . The image dates are chosen to be as late in the ablation season as possible with regards to scene and cloud coverage. As the most northern region is not covered by suitable 2005 Landsat imagery a single scene from 2004 has been used. The method used for extracting glacier lengths is described below. Frontal changes (1985, 2000, 2005, 2010) of three key areas have been chosen for comparison with the 2005 and 2010 ATM/ICESAT data and the 1985 DEM (Figs. S5-7).

Upernavik Ice Stream (fig. S5): Of the four tributary ice streams of the Upernavik Ice Stream system, the most southern ice stream shows considerable thinning at a maximum value of c. 70 m during 1985-2005. This major elevation change is reflected in the frontal position, which retreated c. 2,500 m in the same period, with a majority of the retreat happening between 1985 and 2000. The retreat during 2005-2010 is far less, c. 800 m, which is reflected in a lower vertical change of c. - 25 m. The northern tributary of the Upernavik Ice Stream underwent the opposite development, with little frontal and vertical change during 1985-2005 and a massive retreat (c. 5,500 m) and vertical change (c. 150 m) during 2005-2010. In the entire 1985-2010 period the northern tributary showed a greater thinning than the southern ice stream, with maximum values of c. 180 and 110 m respectively.

Alison Glacier (fig. S6): For Alison Glacier which shows a 1985-2005 thinning with a maximum value of c. 70 m, the position of the calving front was near stationary during 1985-2000, after which the tongue began a rapid retreat lasting until the end of the observation period in 2010. This indicates that the pre-2005 thinning happened mainly between 2000 and 2005, and not before 2000 as

observed in the more southern Upernavik Ice Stream. The unnamed, neighboring glacier north of Alison also shows a considerable pre-2005 thinning at a maximum value of c. 90 m. Here, a large retreat of the front occurred between 1985 and 2000 of c. 3 km and a near stationary 2000-05 position indicates that the main 1985-2005 thinning could have happened before 2000 as for the case of the Upernavik Ice Stream. In the entire 1985-2010 period Alison and its northern, neighboring glacier show maximum thinning rates of c. 120 and 160 m, shifting the maximum thinning from south to north as in the Upernavik case. This corresponds well with the large retreat of the calving front for the unnamed glacier of c. 5 km between 2005 and 2010.

Sverdrup Glacier (fig. S7): The Sverdrup Glacier north of Kjer and Steenstrup glaciers shows a retreat during 1985-2005 of c. 2,500 m with a corresponding surface change of merely - 10 m. The front retreated a further 1,000 m during 2005-2010, while the surface elevation dramatically dropped by 80 m.

Glacier length calculation

To capture the marginal changes in the frontal part of the ice sheet, a new approach to frontal measurements was applied. Using the "AMBUR" program originally developed by Chester P. Jackson Jr. at the Department of Geology and Geography, Georgia Southern University for monitoring shoreline changes, we generated a dense set of measuring lines distanced at 500 meters intervals. Measuring lines are drawn between two transects following the ice sheet margin on either side of the digitized frontal positions (Fig. S8). The lines are first drawn perpendicular to the transects. They are then assigned a new angle to the transect, calculated as the average angle of the four neighboring lines. As a result, each line is parallel to the ice sheet flow and provides information on the frontal changes of this defined area by measuring the length of the glacier along the measuring line. The glacier length extraction was carried out using ESRI's ArcGIS. We applied this analysis to the c. 2000 km ice sheet margin of the entire study area, providing us with c.3600 measuring lines and c.10,000 frontal positions.

ATM data 1994 and 1999

We manually digitized profile lines to the center laser spot track of each of the ATM tracks of 1994 and 1999 (Fig. S1d). We used the snapping functionality of ArcGIS 10.0 so that the line was as close as possible to the center track. Generalization was done by calculating a point on the profile line for every 100 m, then extracting the elevations from the 1985 DEM to the profile line points by bilinear interpolation. We spatially joined the nearest ATM point for 1994 and 1999 to our profile points. Maximum acceptable distance for the spatial join was set to 30 m, yielding an average distance of 13.2 m. Elevation differences were then calculated and the profiles are presented in figures S9 and S10a,b.

Crustal uplift at Thule caused by present-day ice loss

To estimate site coordinates, we use the GIPSY OASIS 6.1 software package(*54*) developed at the Jet Propulsion Laboratory (JPL). We use IGS repro1 satellite orbits, satellite clock parameters, and earth orientation parameters. The repro1

products take the satellite antenna phase center offsets into account. The GPS data was processed as described by Khan et al.(*55*), and align the solutions with the IGS05 frame(*56)*.
The GPS time series contains secular uplift caused by post-glacial rebound (PGR) and uncertainty due to reference frame drift. However, our aim is to detect changes in uplift caused by present-day ice variability. Thus, we fit a trend to data during June 1995 - June 2005 and remove it from the entire data time span.

References

1 Holland, D.M., R.H. Thomas, B. De Young, M.H. Ribergaard, B. Lyberth. Acceleration of Jakobshavn Isbræ triggered by warm subsurface ocean waters. *Nature Geoscience* **1**, 659-664 (2008).

2 Thomas, R.H. *et al*. Investigation of surface melting and dynamic thinning on Jakobshavn Isbræ, Greenland. *Journal of Glaciology* **49**, 231-239 (2003).

3 Howat, I.M. & A. Eddy. Multi-decadal retreat of Greenland's marine-terminating glaciers. *Journal of Glaciology* **57**, 1-8 (2011).

4 Nick, F.M., A. Vieli, I.M. Howat, I. Joughin. Large-scale changes in Greenland outlet glacier dynamics triggered at the terminus. *Nature Geoscience **2***, 110-114 (2009).

5 Pritchard, H.D., R.J. Arthern, D.G. Vaughan, L.A. Edwards. Extensive dynamic thinning on the margins of the Greenland and Antarctic ice sheets. *Nature* **461**, 971-975 (2009).

6 Van den Broeke, M.R. *et al.* Partitioning Recent Greenland Mass Loss. *Science* **326**, 984-986 (2009).

7 Howat, I.M., I. Joughin, T.A. Scambos. Rapid changes in ice discharge from Greenland outlet glaciers. *Science* **315**, 1559-1561 (2007).

8 Khan, S.A., J. Wahr, M. Bevis, I. Velicogna, E. Kendrick. Spread of ice mass loss into northwest Greenland observed by GRACE and GPS. *Geophysical Research Letters* **37** (2010).

9 Velicogna, I. Increasing rates of ice mass loss from the Greenland and Antarctic ice sheets revealed by GRACE. *Geophysical Research Letters* **36** (2009).

10 Joughin, I., B.E. Smith, I.M. Howat, T. Scambos, T. Moon. Greenland flow variability from ice-sheet-wide velocity mapping. *Journal of Glaciology* **56**, 415-430 (2010).

11 AMAP. *The Greenland Ice Sheet in a Changing Climate: Snow, Water, Ice and Permafrost in the Arctic (SWIPA) 2009*. Arctic Monitoring and Assessment Programme (AMAP), Oslo (2009).

12 Rignot, E., I. Velicogna, M.R. van den Broeke, A. Monaghan, J. Lenaerts. Acceleration of the contribution of the Greenland and Antarctic ice sheets to sea level rise. *Geophysical Research Letters* **38**, (2011).

13 Jacob, T., J. Wahr, W.T. Pfeffer, S. Swenson. Recent contributions of glaciers and ice caps to sea level rise. *Nature* (2012) dx.doi.org/10.1038/nature10847.

14 Zwally, H. J., R. Schutz, C. Bentley, J. Bufton, T. Herring, J. Minster, J. Spinhirne, and R. Thomas. 2011. GLAS/ICESat L2 Antarctic and Greenland Ice Sheet Altimetry

Data V031. Boulder, Colorado: NASA Distributed Active Archive Center at the National Snow and Ice Data Center. Digital media.

15 Krabill, W. B., 2010, updated current year, IceBridge ATM L2 Icessn Elevation, Slope, and Roughness, [1993-2010]. Boulder, Colorado USA: NASA Distributed Active Archive Center at the National Snow and Ice Data Center. Digital media. http://nsidc.org/data/ilatm2.html.

16 Ettema, J. *et al*. Higher surface mass balance of the Greenland ice sheet revealed by high-resolution climate modeling. *Geophysical Research Letters* **36** (2009).

17 Ettema, J. *et al*, Climate of the Greenland ice sheet using a high-resolution climate model – Part 1: Evaluation. *The Cryosphere* **4**, 511-527 (2010).

18 Ettema, J., M.R. van den Broeke, E. van Meijgaard, W.J. van de Berg. Climate of the Greenland ice sheet using a high-resolution climate model – Part 2: Near-surface climate and energy balance. *The Cryosphere* **4**, 529-544 (2010).

19 Reeh, N. A nonsteady-state firn-densication model for the percolation zone of a glacier. *Journal of Geophysical Research* **113**, (2008).

20 Reeh, N., D.A. Fisher, R.M. Koerner, H.B. Clausen. An empirical firn-densification model comprising ice lenses. *Annals of Glaciology* **42**, 101-106 (2005).

21 Straneo, F. *et al.* Rapid circulation of warm subtropical waters in a major glacial fjord off East Greenland. *Nature Geoscience* **10**, 182-186 (2010).

22 Murray, T. *et al*. Ocean regulation hypothesis for glacier dynamics in southeast Greenland and implications for ice sheet mass changes. *Journal of Geophysical Research* **115**, (2010).

23 van As, D. Warming, glacier melt and surface energy budget from weather station observations in the Melville Bay region of northwest Greenland. *Journal of Glaciology* **57**, 208 (2011).

24 I. Sasgen *et al.*, Timing and origin of recent regional ice-mass loss in Greenland. *Earth and Planetary Science Letters* **333-334**, 293 (2012).

25 Wahr, J., M. Molenaar, F. Bryan. Time-Variability of Earth's Gravity Field: Hydrological and Oceanic Effects and Their Possible Detection Using GRACE. *Journal of Geophysical Research* **113**, 30.205-30.229 (1998).

26 Carstensen, L.S. & B.V. Jørgensen. Weather and Climate data from Greenland 1958-2010. *DMI Technical Report* **Tr11-10**, (2011).

27 Zwally, H.J. *et al*. Greenland ice sheet mass balance: distribution of increased mass loss with climate warming; 2003 – 07 versus 1992 – 2002. *Journal of Glaciology* **57**, 88-102 (2011).

28 Ewert, H. *et al*. Volume and mass changes of the Greenland ice sheet inferred from ICESat and GRACE. *Journal of Geodynamics* (2011). doi:10.1016/j.jog.2011.06.003.

29 Chen, J. L., C.R. Wilson, B.D. Tapley. Interannual variability of Greenland ice losses from satellite gravimetry, *Journal of Geophysical Research* **116** (2011).

30 Wouters, B., D. Chambers, E.J.O Schrama. GRACE observes small-scale mass loss in Greenland. *Geophysical Research Letters* **35** (2008).

31 Ground control for 1:150,000 scale aerials, Greenland. *Danish Ministry of the Environment – National Survey and Cadastre,* (2012, June 8)

http://www.kms.dk/Emner/Landkortogtopografi/Flyfotos/Daekningsomraader_i_Groenland/Ground_control_Greenland.htm

32 GR96 - det grundlæggende 3D-referencesystem i Grønland. *Danish Ministry of the Environment – National Survey and Cadastre,* (2012, June 8) http://www.kms.dk/Emner/Referencenet/Referencesystemer/GR96/GR96.htm

33 REFGR on Greenland. *Danish Ministry of the Environment – National Survey and Cadastre,* (2012, June 8) http://www.kms.dk/English/Geodesy+and+Surveying/Reference+Networks/REFGR+on+Greenland/

34 Next-Generation Automatic Terrain Extraction (NGATE) – Innovation in the cost-effective derivation of elevation data from imagery. *BAE SYSTEMS* http://www.socetset.com/docs/education/white_papers/wp_ngate.pdf

35 Krabill, W.B. *et al*. Aircraft laser altimetry measurement of elevation changes of the Greenland ice sheet: technique and accuracy assessment. *Journal of Geodynamics* **34**, 357-376 (2002).

36 Guidelines for Digital Elevation Data, version 1.0. *National Digital Elevation Program* http://www.ndep.gov/NDEP_Elevation_Guidelines_Ver1_10May2004.pdf

37 Motyka, R.J., M. Fahnestock, M. Truffer. Volume change of Jakobshavn Isbræ, West Greenland: 1985-1997-2007. *Journal of Glaciology* **56**, 198, (2010).

38 Korona, J., E. Berthier, M. Bernard, F. Rémy, E. Thouvenot. SPIRIT. SPOT 5 stereoscopic survey of Polar Ice: Reference Images and Topographies during the fourth International Polar Year (2007-2009). *ISPRS Journal of Photogrammetry and Remote Sensing* **64**, 204-212 (2009).

39 Jacobsen, K. DEM generation by SPOT HRS. International Archives of photogrammetry. *Remote Sensing and Spatial Information Sciences* **35**, 439-444 (2004).

40 Yi, D., H.J. Zwally, X. Sun. ICESat measurement of Greenland ice sheet surface slope and roughness. *Annals of Glaciology* **42**, (2005).

41 Luthcke, S. B., D.D. Rowlands, T.A. Williams, & M. Sirota. Calibration and reduction of ICESat geolocation errors and the impact on ice sheet elevation change detection. Geophysical Research Letters **32**, (2005).

42 Fricker, H. A. *et al.* Assessment of ICESat performance at the salar de Uyuni, Bolivia. *Geophysical Research Letters* **32** (2005).

43 Howat, I. M., B.E. Smith, I. Joughin, T.A. Scambos. Rates of southeast Greenland ice volume loss from combined ICESat and ASTER observations, *Geophysical Research Letters* **35** (2008).

44 Heiskanen, W.A. & H. Moritz. *Physical Geodesy* (W.H. Freeman, San Francisco, 1967).

45 Forsberg, R. & C.C. Tscherning. An overview manual for the GRAVSOFT, Geodetic Gravity Field Modelling Programs, 2.edition August 2008, Niels Bohr Institute, University of Copenhagen (2008)
46 Cheng, M. K. & B.D. Tapley. Variations in the Earth's oblateness during the past 28 years, *Journal of Geophysical Research* **109** (2004).
47 Swenson, S., D. Chambers, J. Wahr. Estimating Geocenter Variations from a Combination of GRACE and Ocean Model Output. *Journal of Geophysical Research* **113** (2008).
48 Velicogna, I. & J. Wahr. Acceleration of Greenland ice mass loss in spring 2004. *Nature* **443**, 329-331 (2006).
49 Chen, J.L, C.R. Wilson, B.D. Tapley. Satellite Gravity Measurements Confirm Accelerated Melting of Greenland Ice Sheet. *Science* **313**, 1958-1960 (2006).
50 Luthcke, S.B. et al. Recent Greenland Ice Mass Loss by Drainage System from Satellite Gravity Observations. *Science* **314**, 1286-1289 (2006).
51 Rignot, E., J.E. Box, E. Burgess, E. Hanna. Mass balance of the Greenland ice sheet from 1958 to 2007. *Geophysical Research Letters* **35**, (2008).
52 Reeh, N. Parameterization of melt rate and surface temperature on the Greenland Ice Sheet. *Polarforschung* **5913**, 113-128 (1991).
53 Zwally, H.J., J. Li. Seasonal and interannual variations of firn densification and ice-sheet surface elevation at the Greenland summit. *Journal of Glaciology* **48** (161), 199-207 (2002).
54 Zumberge, J.F., M.B. Heflin, D.C. Jefferson, M.M. Watkins, F.H. Webb. Precise point positioning for the efficient and robust analysis of GPS data from large networks. *Journal of Geophysical Research* **102**, (1997).
55 Khan, S. A., L. Liu, J. Wahr, I.M. Howat, I. Joughin, T. van Dam, K. Fleming. GPS measurements of crustal uplift near Jakobshavn Isbræ due to glacial ice mass loss. *Journal of Geophysical Research* **115**, (2010).
56 Altamimi, Z., X. Collilieux, J. Legrand, B. Garayt, C. Boucher. ITRF2005: A new release of the International Terrestrial Reference Frame based on time series of station positions and Earth Orientation Parameters, *Journal of Geophysical Research* **112** (2007).

Fig S1

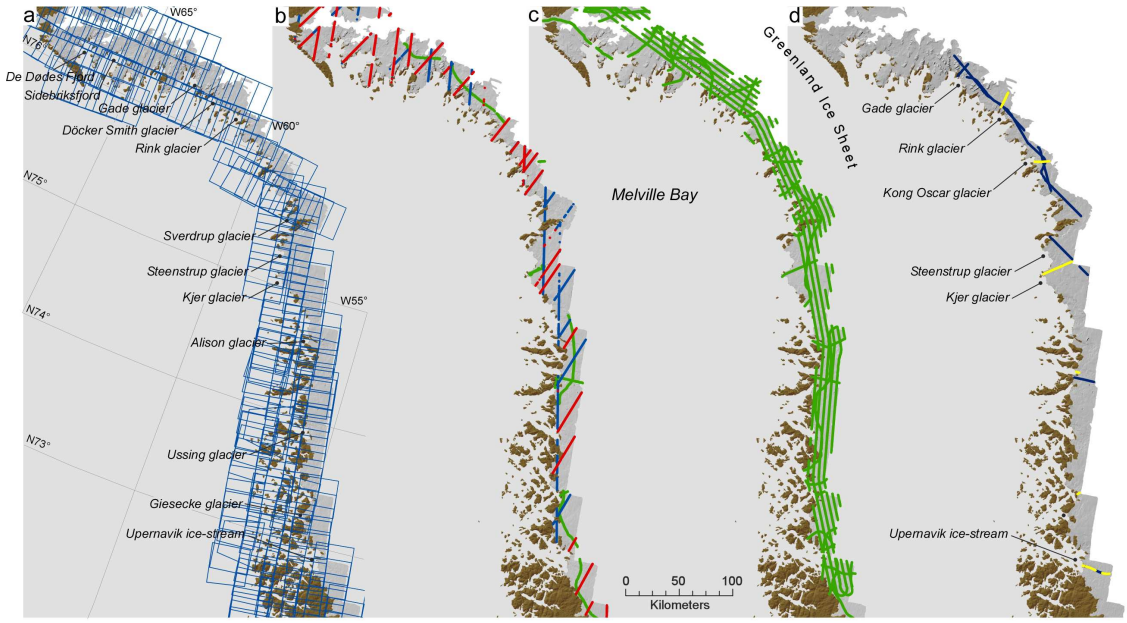

Data coverage for elevation estimates. a. Footprint coverage of aerial photographs recorded in 1985 by the Danish National Survey and Cadastre (KMS). b. ICESat (red and blue) and ATM (green) from 2005. c. ATM (green) from 2010. d. ATM data from 1994 (yellow) and 1999 (blue).

Fig S2

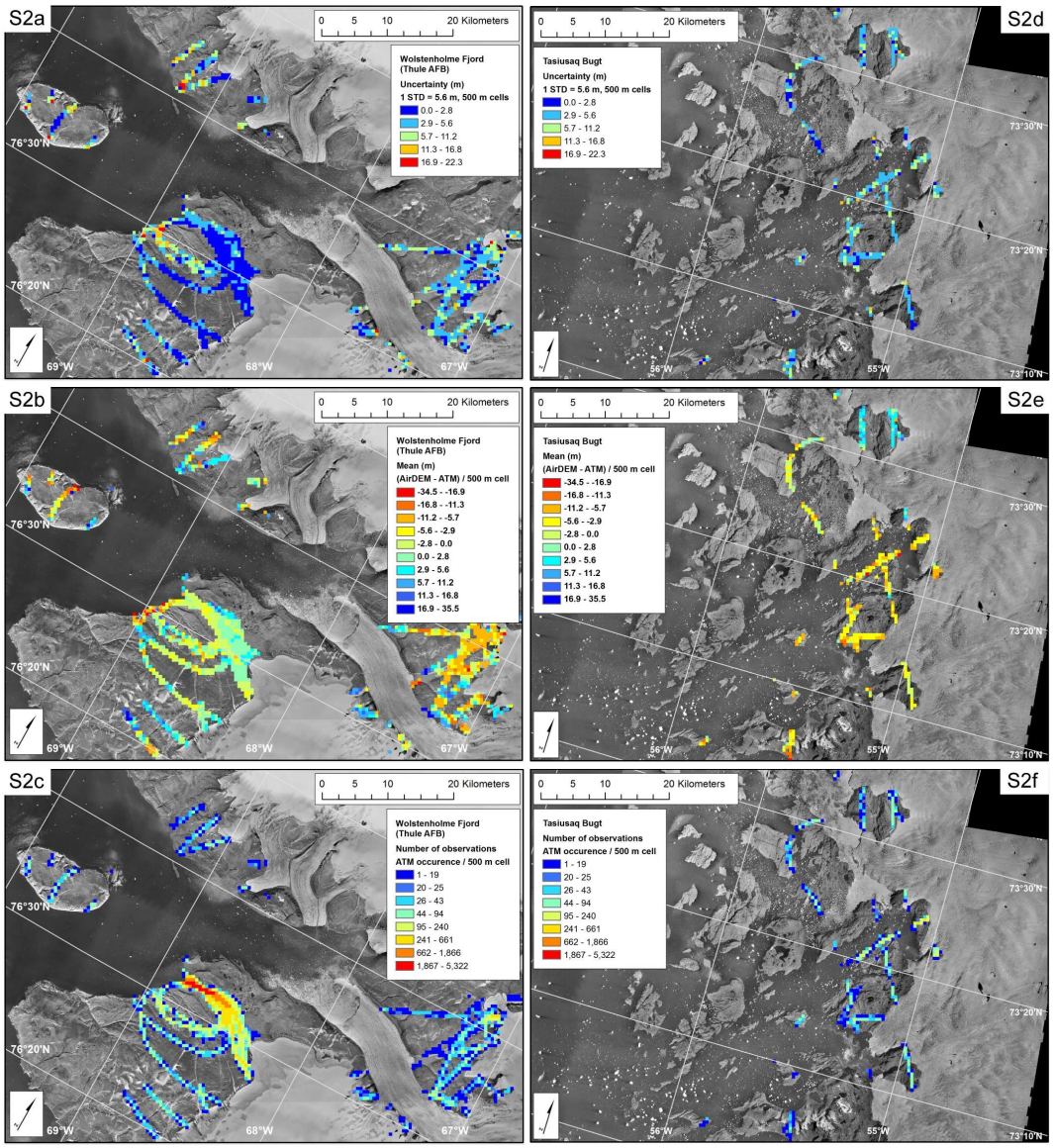

DEM1985-ATM validation. Two locations displaying the non-slope-filtered data generalized into 500 m cell statistics. Figs. S2a-c. Wolstenholme Fjord (Thule AFB) has an atypically high density of sample points and shows some erratic behavior in the eastern half, possibly related to the process of image correlation when measuring elevations by the program. Figs. S2d-f. Tasiusaq Bugt has a more even and typical distribution of sample points.

Fig S3

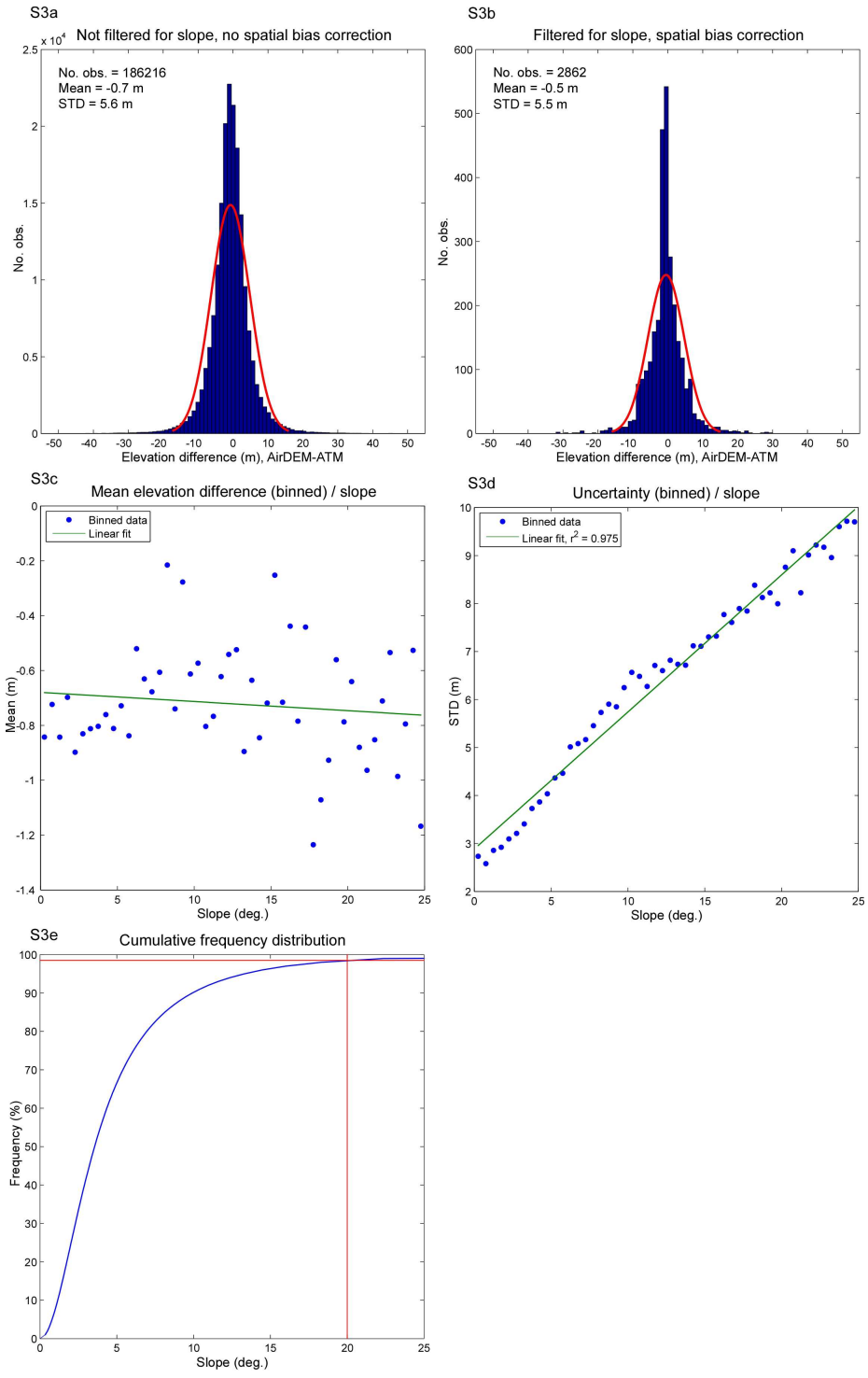

Statistics of the tested data shown in Figs. S2a-f. Fig. S3a. Frequency distribution of the raw, unfiltered elevation differences on stable terrain, e.g. bedrock (including nunataks). AirDEM (1985) is validated with reference to ATM tracks. The red line denotes a Gaussian fit. Fig. S3b. Frequency distribution of elevation differences after slopes greater than 20 degrees have been excluded and also corrected for spatial bias. The negative bias of 0.5 m has been used to adjust the model and $\sigma_{terrain}$ = 5.5 m is the uncertainty of the ice-free terrain. Fig. S3c. Mean

elevation difference (AirDEM – ATM) plotted against corresponding bedrock slope values in 0.5 degree bins, illustrating the random nature of bias as a function of slope. The linear fit denotes how the mean is slightly decreasing with slope. The same data as for Fig. S3a. Fig. S3d. Uncertainty (σ= STD) of the elevation differences (AirDEM – ATM) plotted against bedrock slope values in 0.5 degree bins. The least squares linear fit result is: y = 0.2855x + 2.8865, based on 0.5 degree bins and an interval of [0; 25] degrees. r^2 = 0.975. The same data as for Fig. S3a. Fig. S3e Cumulative frequency distribution for slope values on the inland ice land coverage. Only pixels which have a measured height have been included. The y-axis plots percentages (quantiles) of all included slope values of the ice. The red lines mark the quantile (98.5%) at a slope value of 20 degrees. Thus, 98.5% of the ice-covered area has slope values below 20 degrees. With the linear least squares fit formula from Fig. S3d, this is the input to the surface slope correction of the $\sigma_{terrain}$ = 5.5 m to σ_{ice} = 4.1 m.

Fig S4

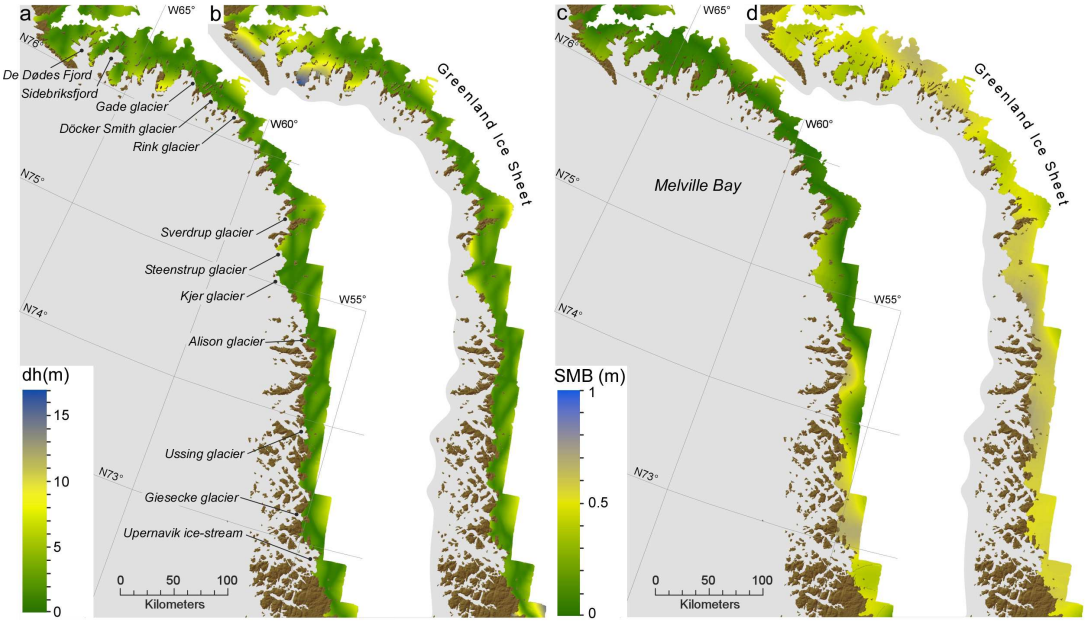

Figure S4, Supplementary, Kjær et al.

Uncertainty related to interpolation and elevation differences. a. dh1985-2005. b. dh2005-2010. c. SMB 1985-2005 d. SMB 2005-2010.

Fig S5

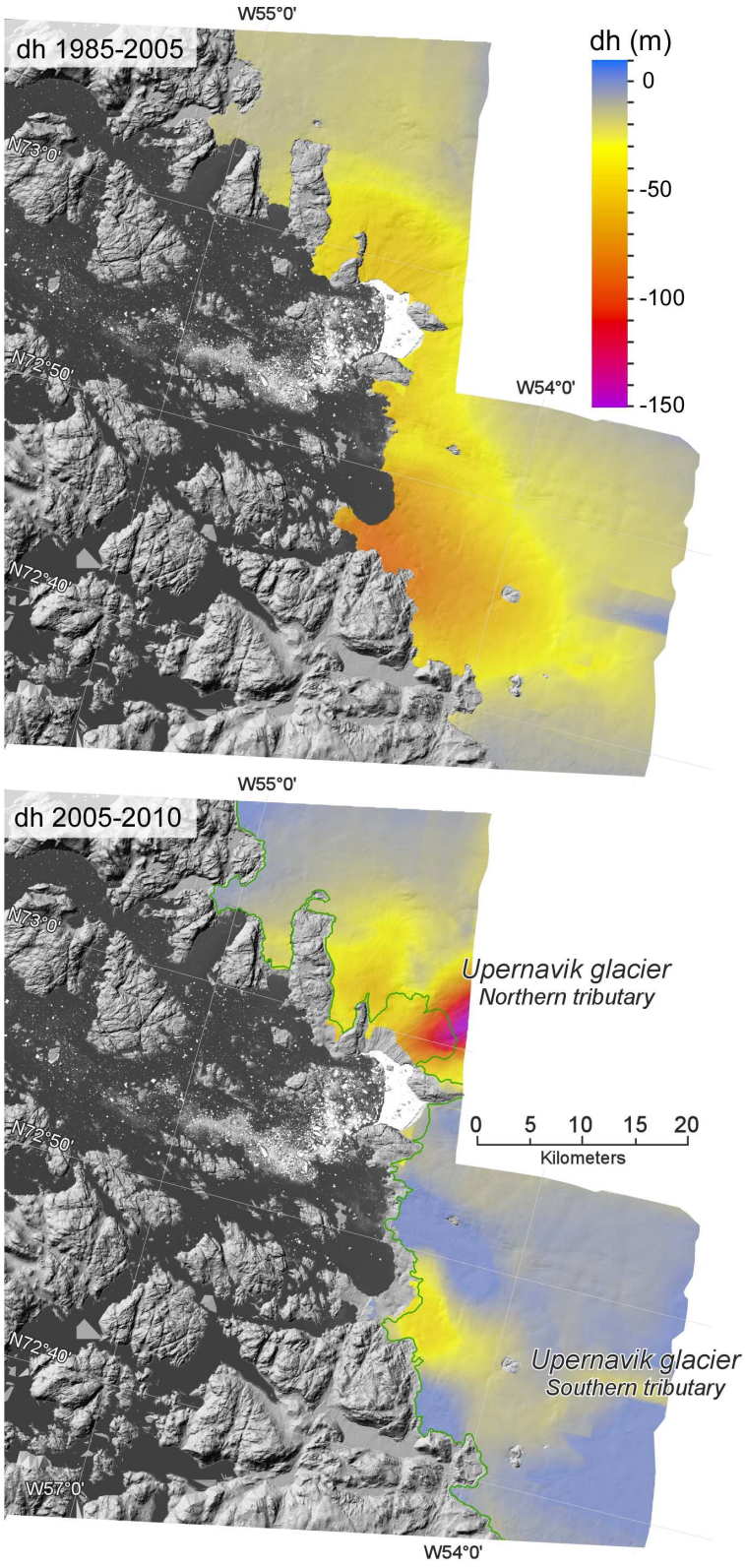

Elevation difference (dh) adjacent to the Upernavik Ice stream (area 1).

Fig S6

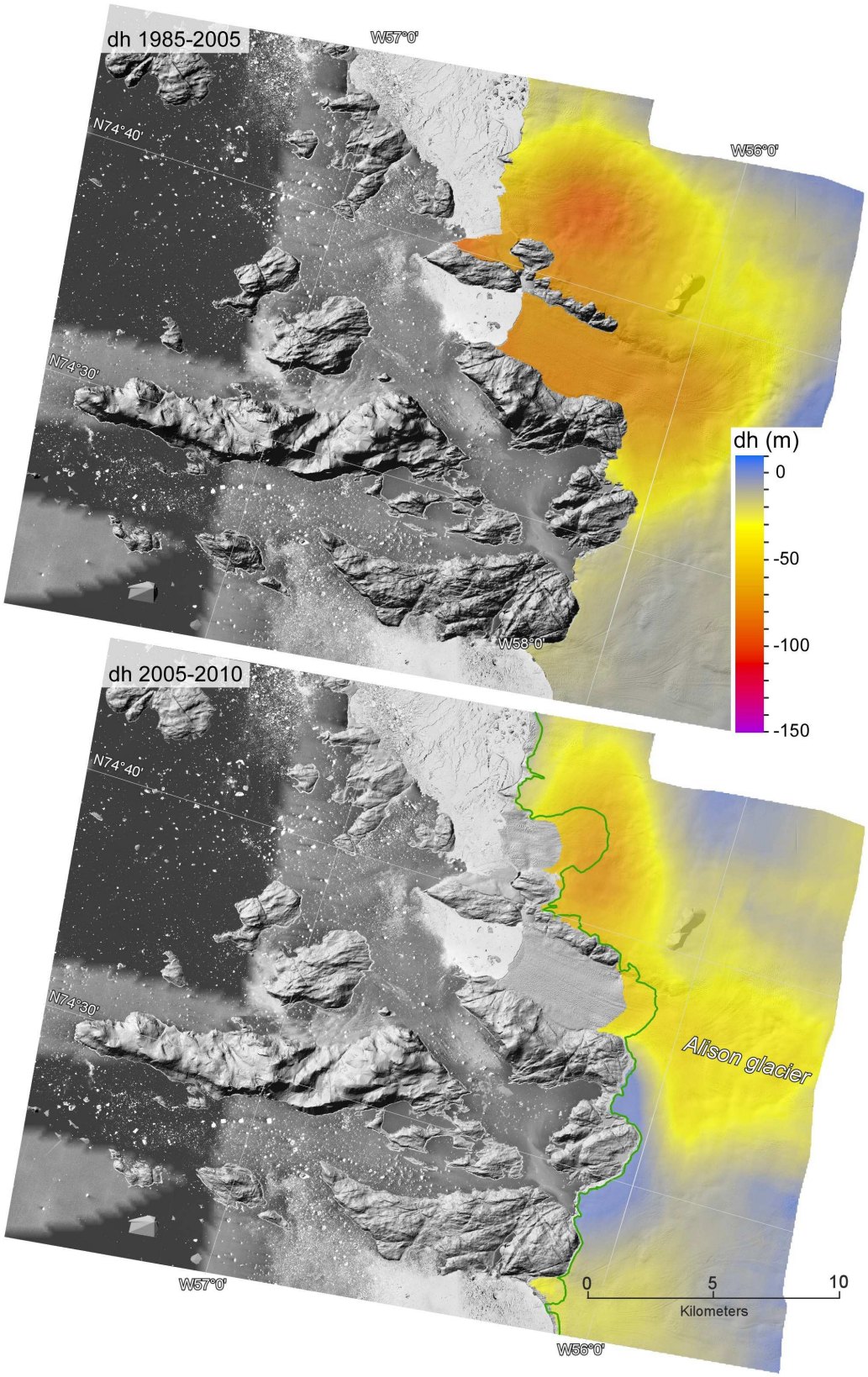

Elevation difference (dh) adjacent to the Alison glacier (area 2).

Fig S7

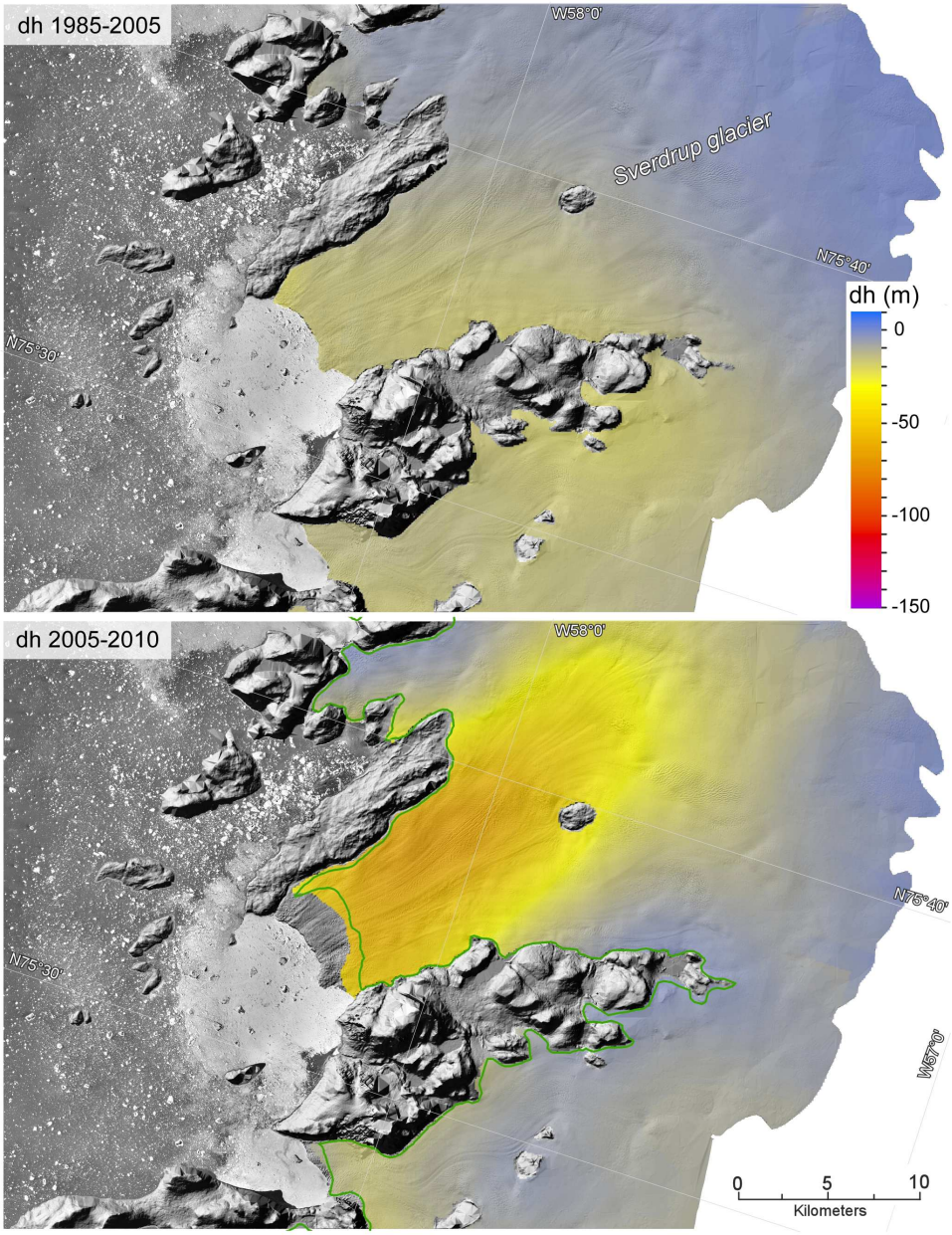

Elevation difference (dh) adjacent to the Sverdrup glacier (area 3).

Fig S8

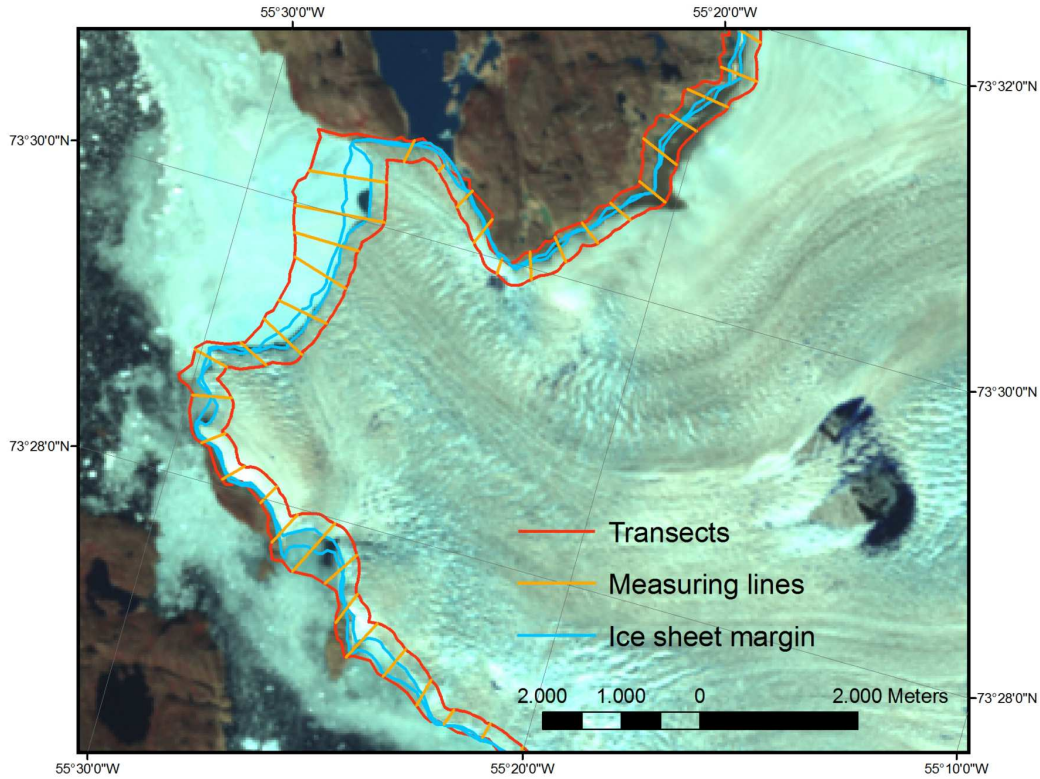

Illustration of method used to measure glacier lengths. Measuring lines (orange) are drawn automatically between transects (red). Glacier lengths are measured from the inner transect to the digitized ice margin (blue). Example from southern Giesecke glacier with measuring lines for every 500 m along the transect. Background image is a Landsat-scene from August 2010 (L71017008-0082010814).

Fig S9

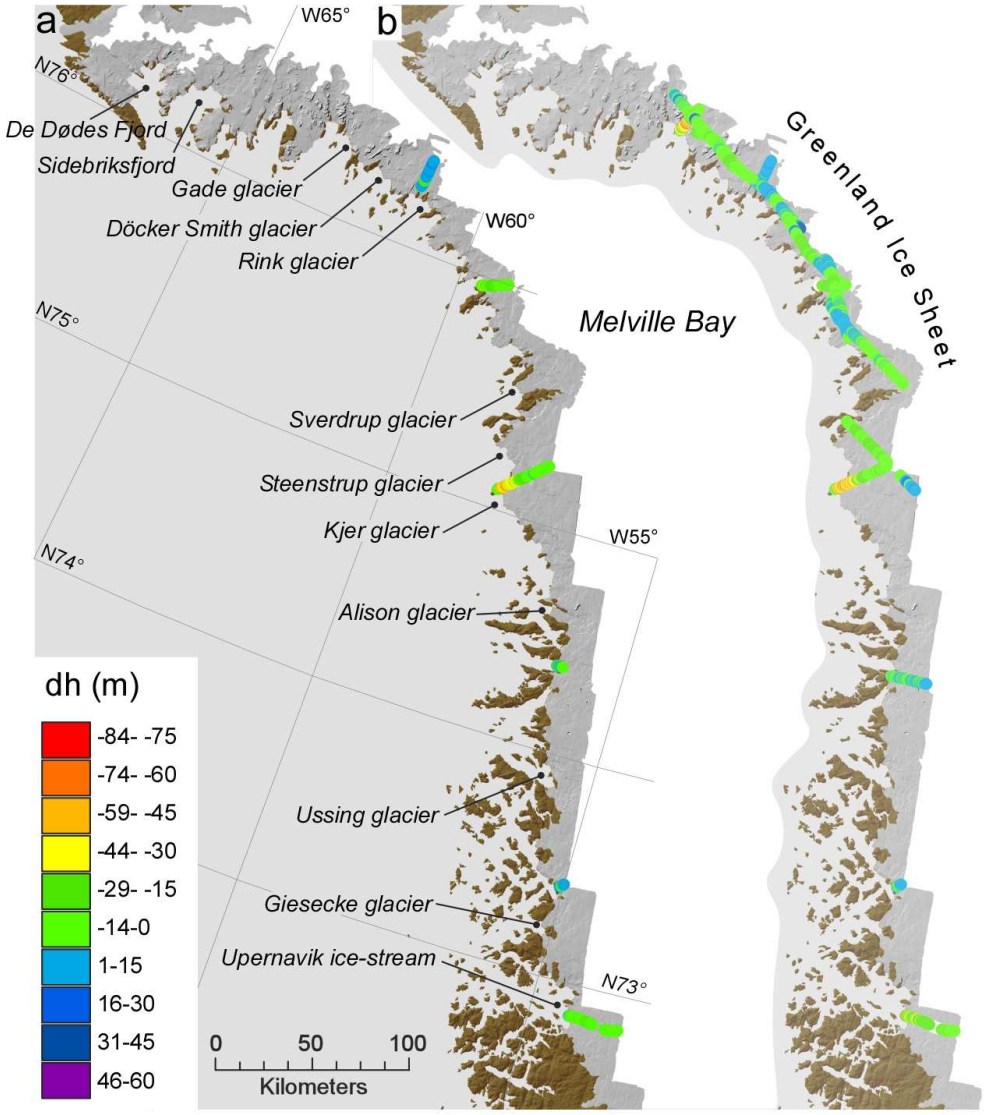

Elevation difference (dh) between 1985 and 1990s based on the aerial DEM and ATM data. a. Flight lines from 1994 b. Flight line from 1999.

Fig S10

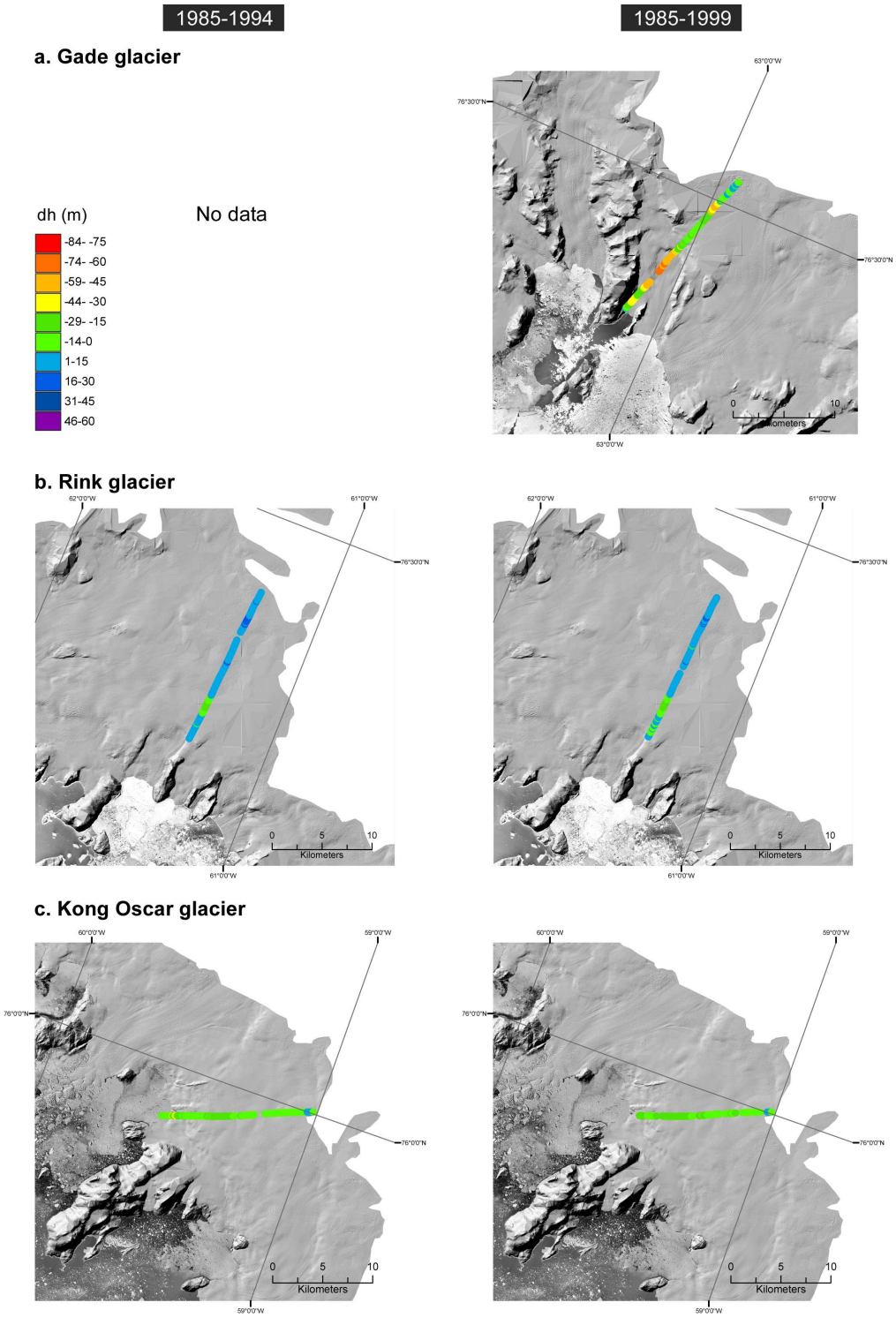
1985-1994
1985-1999
a. Gade glacier
dh (m)
-84- -75
-74- -60
-59- -45
-44- -30
-29- -15
-14-0
1-15
16-30
31-45
46-60
No data
b. Rink glacier
c. Kong Oscar glacier
Kilometers

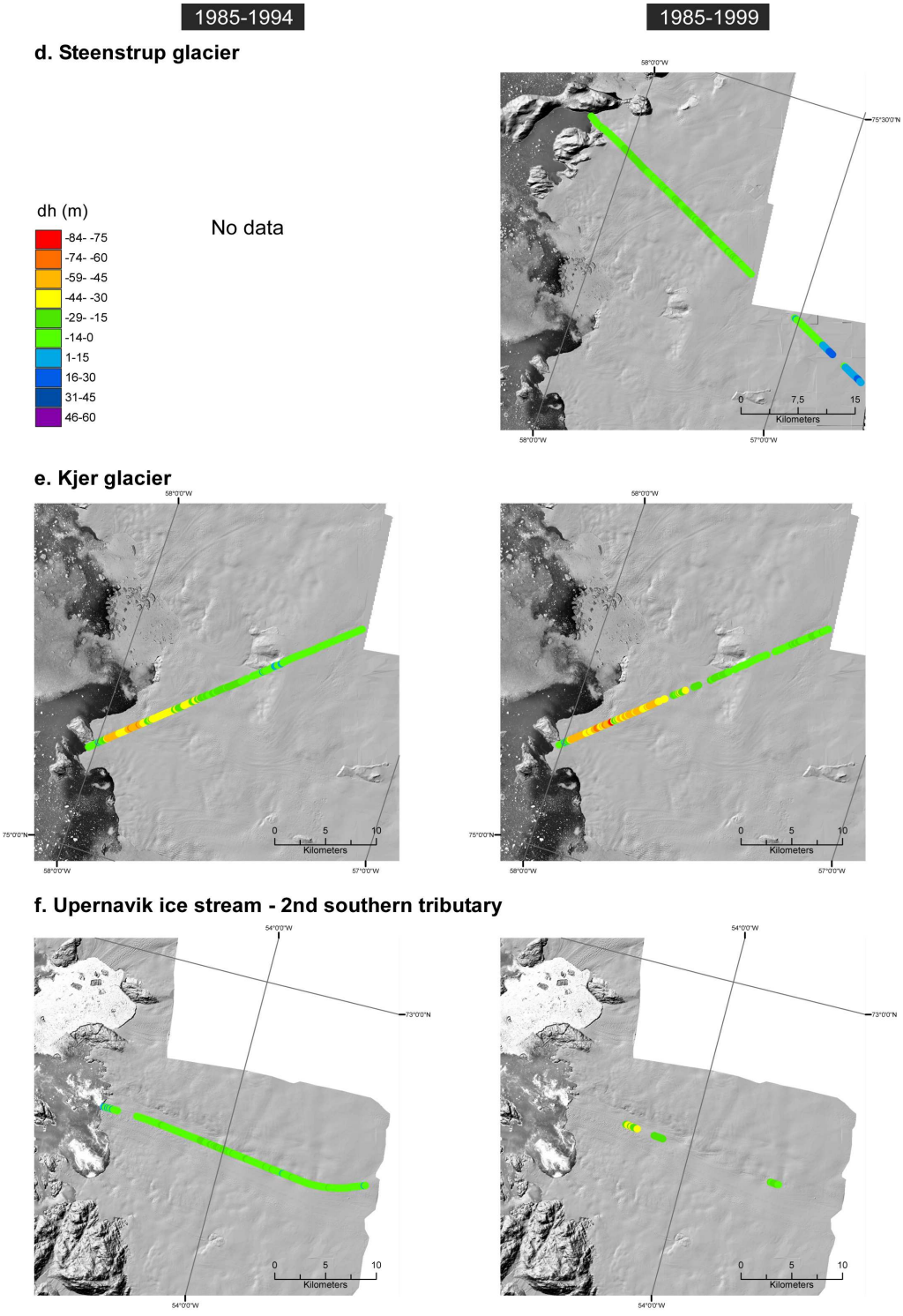

ATM data from 1994 and 1999 superimposed on 1985 DEM shown as a shaded relief. a. Gade Glacier, b. Rink glacier, c. Kong Oscar glacier, d. Steenstrup glacier, e. Kjer, f. Upernavik, 2nd southern tributary.